

# Simulation of the physical properties of the chalcogenide glass $\text{As}_2\text{S}_3$ using a density-functional-based tight-binding method

S. I. Simdyankin\* and S. R. Elliott  
*Department of Chemistry, University of Cambridge,  
Lensfield Road, Cambridge CB2 1EW, United Kingdom*

Z. Hajnal, T. A. Niehaus, Th. Frauenheim  
*Fachbereich 6 — Theoretische Physik, Universität Paderborn,  
Warburger Straße 100, D-33098, Paderborn, Germany*  
(Dated: March 24, 2018)

We have used a density-functional-based tight-binding method in order to create structural models of the canonical chalcogenide glass, amorphous (a-)  $\text{As}_2\text{S}_3$ . The models range from one containing defects that are both chemical (homopolar bonds) and topological (valence-alternation pairs) in nature to one that is defect-free (stoichiometric). The structural, vibrational and electronic properties of the simulated models are in good agreement with experimental data where available. The electronic densities of states obtained for all models show clean optical band gaps. A certain degree of electron-state localization at the band edges is observed for all models, which suggests that photoinduced phenomena in chalcogenide glasses may not necessarily be attributed to the excitation of defects of only one particular kind.

## I. INTRODUCTION

Amorphous chalcogenides (particularly the sulfides, selenides and tellurides) exhibit intriguing physical properties that are not observed in their crystalline counterparts. Some of these unusual properties are extensively used in electronic and photonic devices<sup>1</sup> and there are many potential applications.

Perhaps the most interesting opto-electronic behavior of these materials is the metastable structural changes resulting from the absorption of near-bandgap light<sup>2</sup>. The microscopic changes in the atomic structure involved are not generally observable directly, but they are reflected in measurable optical, electronic, and mechanical properties<sup>3,4</sup>. A fully consistent microscopic theory accounting for the opto-electronic behavior in chalcogenide glasses, however, is still lacking. It is therefore of great interest to employ computer simulations in order to generate and study structural models of such materials. Provided that these computer-generated models compare well with available experimental data, they could allow one to monitor the photo-induced structural changes in the greatest possible detail at the microscopic level. Needless to say, such detailed information is not generally presently available from experiments.

In order to study opto-electronic effects, one needs to perform quantum-mechanical calculations that are very time consuming. This imposes a severe constraint on the accessible system size of the simulated models. It is possible, however, that small samples may be sufficient to capture much of the interesting photoinduced behavior due to a high degree of localization of the photo-excited electron-hole pairs<sup>5,6</sup>. A few *ab initio* studies of amorphous chalcogenides, paying particular attention to electronic properties, have been performed by Drabold and co-workers (see, e.g., Refs. 7,8,9). Although their results agree well with experimental data, the defect concentra-

tion in these structural models is much greater than is estimated in experiments. Some of the possible reasons for this are the level of approximation in the *ab initio* approach employed in these studies and/or the model preparation history, which may have resulted in too many quenched-in defects due to very rapid cooling of the sample from the liquid state.

In this paper, we use a density-functional-based tight-binding (DFTB) method<sup>10</sup> in order to generate and analyze several models of amorphous diarsenic trisulphide (a- $\text{As}_2\text{S}_3$ ) with a controlled and systematic change in the defect concentration. Apart from being widely regarded as the canonical chalcogenide glass, this particular material was chosen for analysis for the following reasons. First, we have obtained reliable high-quality neutron-scattering structural data for this material<sup>11,12</sup>. Second, the properties of a- $\text{As}_2\text{S}_3$  are expected to be similar to those of a- $\text{As}_2\text{Se}_3$ , amorphous diarsenic triselenide, that have been studied theoretically in Ref. 8, and it is of interest to corroborate this similarity in independent simulations. Third, the necessary input DFTB data for sulphur have been previously generated and extensively tested<sup>13</sup>.

Although the DFTB method is semiempirical, it allows one to improve upon the standard tight-binding description of interatomic interactions by including a DFT-based self-consistent second order in charge fluctuation (SCC) correction to the total energy. The flexibility in choosing the desired accuracy while computing the interatomic forces brings about the possibility to perform much faster calculations when high precision is not required, and refine the result if needed.

## II. METHODOLOGY

### A. DFTB

The SCC-DFTB model is derived from density-functional theory (DFT) by a second-order expansion of the DFT total energy functional with respect to the charge-density fluctuations  $\delta n' = \delta n(\vec{r}')$  around a given reference density  $n'_0 = n_0(\vec{r}')$ :

$$\begin{aligned}
 E &= \sum_i^{occ} \langle \Psi_i | \hat{H}^0 | \Psi_i \rangle \\
 &+ \frac{1}{2} \iint' \left( \frac{1}{|\vec{r} - \vec{r}'|} + \left. \frac{\delta^2 E_{xc}}{\delta n \delta n'} \right|_{n_0} \right) \delta n \delta n' \quad (1) \\
 &- \frac{1}{2} \iint' \frac{n'_0 n_0}{|\vec{r} - \vec{r}'|} + E_{xc}[n_0] - \int V_{xc}[n_0] n_0 + E_{ii},
 \end{aligned}$$

where  $\int d\vec{r}'$  is expressed by  $\int'$ . Here,  $\hat{H}^0 = \hat{H}[n_0]$  is the effective Kohn-Sham Hamiltonian evaluated at the reference density and the  $\Psi_i$  are Kohn-Sham orbitals.  $E_{xc}$  and  $V_{xc}$  are the exchange-correlation energy and potential, respectively and  $E_{ii}$  is the core-core repulsion energy.

To derive the total energy of the SCC-DFTB method, the energy contributions in Eq. (1) are further subjected to the following approximations:

1) The Hamiltonian matrix elements  $\langle \Psi_i | \hat{H}^0 | \Psi_i \rangle$  are represented in a minimal basis of confined, pseudoatomic orbitals  $\phi_\mu$ ,

$$\Psi_i = \sum_\mu c_\mu^i \phi_\mu.$$

To determine the basis functions  $\phi_\mu$ , we solve the atomic DFT problem by adding an additional harmonic potential  $(\frac{r}{r_0})^2$  to confine the basis functions<sup>14</sup>. The Hamiltonian matrix elements in this LCAO basis,  $H_{\mu\nu}^0$ , are then calculated as follows. The diagonal elements  $H_{\mu\mu}^0$  are taken to be the atomic eigenvalues and the non-diagonal elements  $H_{\mu\nu}^0$  are calculated in a two-center approximation:

$$H_{\mu\nu}^0 = \langle \phi_\mu | \hat{T} + v_{eff}[n_\alpha^0 + n_\beta^0] | \phi_\nu \rangle \quad \mu \in \alpha, \nu \in \beta,$$

which are tabulated, together with the overlap matrix elements  $S_{\mu\nu}$  with respect to the interatomic distance  $R_{\alpha\beta}$ .  $v_{eff}$  is the effective Kohn-Sham potential and  $n_\alpha^0$  are the densities of the neutral atoms  $\alpha$ .

2) The charge-density fluctuations  $\delta n$  are written as a superposition of atomic contributions  $\delta n_\alpha$ ,

$$\delta n = \sum_\alpha \delta n_\alpha,$$

which are approximated by the charge fluctuations at the atoms  $\alpha$ ,  $\Delta q_\alpha = q_\alpha - q_\alpha^0$ .  $q_\alpha^0$  is the number of electrons of the neutral atom  $\alpha$  and the  $q_\alpha$  are determined from

a Mulliken-charge analysis. The second derivative of the total energy in Eq. (1) is approximated by a function  $\gamma_{\alpha\beta}$ , whose functional form for  $\alpha \neq \beta$  is determined analytically from the Coulomb-interaction of two spherical charge distributions, located at  $R_\alpha$  and  $R_\beta$ . For  $\alpha = \beta$  it represents the electron-electron self-interaction on atom  $\alpha$ .

3) The remaining terms in Eq. (1),  $E_{ii}$  and the energy contributions, which depend on  $n_0$  only, are collected in a single energy contribution  $E_{rep}$ .  $E_{rep}$  is then approximated as a sum of short-range repulsive potentials,

$$E_{rep} = \sum_{\alpha \neq \beta} U[R_{\alpha\beta}],$$

which depend on the interatomic distances  $R_{\alpha\beta}$ .

With these definitions and approximations, the SCC-DFTB total energy finally reads:

$$E_{tot} = \sum_{i\mu\nu} c_\mu^i c_\nu^i H_{\mu\nu}^0 + \frac{1}{2} \sum_{\alpha\beta} \gamma_{\alpha\beta} \Delta q_\alpha \Delta q_\beta + E_{rep}. \quad (2)$$

Applying the variational principle to the energy functional (2), one obtains the corresponding Kohn-Sham equations:

$$\sum_\nu c_{\nu i} (H_{\mu\nu} - \epsilon_i S_{\mu\nu}) = 0, \quad \forall \mu, i \quad (3)$$

$$H_{\mu\nu} = \langle \phi_\mu | H_0 | \phi_\nu \rangle + \frac{1}{2} S_{\mu\nu} \sum_\zeta (\gamma_{\alpha\zeta} + \gamma_{\beta\zeta}) \Delta q_\zeta,$$

which have to be solved iteratively for the wavefunction expansion coefficients  $c_\mu^i$ , since the Hamiltonian matrix elements depend on the  $c_\mu^i$  due to the Mulliken charges. Analytic first derivatives for the calculation of interatomic forces are readily obtained, and second derivatives of the energy with respect to atomic positions are calculated numerically.

The repulsive pair potentials  $U[R_{\alpha\beta}]$  are constructed by subtracting the DFT total energy from the SCC-DFTB electronic energy (first two terms on the right-hand side of eq.(2)) with respect to the bond distance  $R_{\alpha\beta}$  for a small set of suitable reference systems.

To sum up, in order to parameterize the method for a new element, the following steps have to be taken. First, DFT calculations have to be performed for the neutral atom to determine the LCAO basis functions  $\phi_\mu$  and the reference densities  $n_\alpha^0$ . Here the confinement radius can in principle be chosen different for the density ( $r_0^n$ ) and each type of atomic orbital ( $r_0^{s,p,d}$ ). We usually take  $r_0$  to be the same for s- and p-functions. In a minimal basis, this yields a total number of two adjustable parameters for elements in the first and second rows, while there are three if d-functions are included. After this, the different matrix elements can be calculated and the pair potentials  $U[R_{\alpha\beta}]$  are obtained as stated above for every combination of the new element with the ones already parameterized.

In this study, we used the same tabulated data set for sulphur-sulphur interactions as in Ref. 13, and the As-As, As-S and S-As data sets were generated according to the procedure outlined above. The confinement radii for the As pseudoatomic densities ( $r_d = 9.8$  a.u. and  $r_w = 4.5$  a.u.), as well as the As-As repulsive pair-potential were determined in accord with other ongoing efforts related to GaAs systems. The cage-like  $\text{As}_4\text{S}_6$  molecule was used to calculate the As-S repulsive pair potential, so that after finding the minimum energy configuration of the molecule in all-electron DFT-LDA calculations using the NRLMOL program<sup>15</sup>, a regular scaling of the As-S bond-lengths was performed, keeping the overall  $T_d$  symmetry. Then the acquired potentials were tested on other clusters, such as  $\text{As}_2\text{S}$  and  $\text{As}_4\text{S}_4$  molecules, with an overall good agreement of the binding energies and configurations between SCC-DFTB and the reference all-electron DFT-LDA NRLMOL results. When these data sets were used in order to optimize the geometry of the crystal structure of orpiment (*c*- $\text{As}_2\text{S}_3$ ) in SCC-DFTB, the agreement with the experimental structure<sup>16</sup> was within 2%.

## B. Preparation of structural models

In experiments, bulk glasses are usually prepared from the melt by rapidly cooling (quenching) the sample. Although it appears impossible to achieve experimentally realistic cooling rates in molecular-dynamics computer simulations, some empirical procedures result in models that can be in good agreement with experiments. In order to prepare realistic models of *a*- $\text{As}_2\text{S}_3$ , we use an algorithm akin to that used, e.g., in Refs. 7,8,17.

The structural model of *a*- $\text{As}_2\text{S}_3$  was obtained in the course of an *NVT* (constant number of particles,  $N$ , volume,  $V$ , and temperature,  $T$ ) molecular-dynamics simulation with periodic boundary conditions. Since we are not interested in statistical properties of thermal fluctuations, the temperature was controlled simply by scaling the velocities of the constituent particles every few time steps with the time intervals between the scalings taken randomly with a mean value of 10 time steps. We used a time step of 100 a.u.  $\approx 2.4$  fs (1 a.u. =  $2.4189 \times 10^{-17}$  s) and the Verlet algorithm in order to integrate the equations of motion.

The starting configuration was a system of 200 (80 arsenic and 120 sulphur) atoms in a cubic supercell, with a side length of 17.25 Å, obtained by rescaling a crystalline configuration of orpiment (monoclinic, space group 14,  $P12_1/n1$ ) with  $1 \times 2 \times 5$  20-atom unit cells. The crystalline coordinates were obtained from the Inorganic Crystal Structure Database and correspond to those reported in Ref. 16. In order to obtain a cubic supercell, we approximated the monoclinic unit cell of orpiment by an orthorhombic one simply by neglecting the small deviation of the angle  $\beta = 90.68^\circ$  from the right angle. Then we used the experimental glass density of  $\rho = 3.186$  g/cm<sup>3</sup>

from Ref. 18 in order to obtain the side length of the cubic supercell  $L = (N/\rho)^{1/3} = 17.25$  Å and the coordinates of atoms from the cuboid with dimensions 11.48 by 19.15 by 21.28 Å were scaled by 1.5, 0.9, and 0.81 in the  $x$ ,  $y$ , and  $z$  directions, respectively. The use of the crystalline initial configuration gives the correct stoichiometry and the rescaling of a non-cubic supercell in order to obtain a cubic one serves the goal of eliminating possible anisotropies in physical properties. Note that in Ref. 8, the authors cut a cubic supercell from a crystalline phase of  $\text{As}_2\text{Se}_3$  isostructural to orpiment, thus achieving the above two goals, but disrupting the periodicity with respect to the periodic boundary conditions. After thorough equilibration in the simulated liquid state, however, the use of either of these two prescriptions should lead to models with similar statistical properties.

The initial configuration was melted and equilibrated first at  $T = 3000$  K for 3 ps, and then the resulting configuration was allowed to equilibrate at  $T = 1000$  K for 12 ps. The equilibration criterion used was the convergence of the average potential energy to a constant value. At such high temperatures, the accuracy of the calculations appears to be least significant for the subsequent generation of low-temperature structural models. Therefore, at this stage, a minimal basis set of only s and p orbitals on both the As and S atoms was used, and the tight-binding scheme of Sec. II A was used without the self-consistent charge (SCC) correction in order to speed up the calculations. It was necessary, however, to use the SCC correction during the initial 1.5 ps of the  $T = 3000$  K run, since the large forces resulting from the presence of small interatomic distances in the distorted starting configuration otherwise led to numerical instability.

While preparing computer-generated models of glasses, it is customary to mimic real experiments by reducing the temperature over time intervals whose length, however, is limited by the available computer time. We found that, due to the unrealistically small length of such time intervals, this approach is rather impractical. Instead, we used the available computer time to perform an annealing run at one fixed temperature which is low enough for the process of the bond-network formation to be activated and high enough for the topologically connected network to grow sufficiently rapidly. First, we performed a run corresponding to 6 ps at  $T = 700$  K with the SCC correction and the minimal (sp) basis. Keeping in mind that the simulation was done at constant volume, this temperature was chosen to be somewhat above the melting temperature of orpiment at atmospheric pressure ( $T_m = 592$  K according to Ref. 19). We empirically found that annealing the configuration for the following 6 ps at a higher temperature of  $T = 800$  K slightly improved the quality of the network by increasing the fraction of heteropolar bonds in the model. During these two runs, we used a smaller time step of 50 a.u. (1.2 fs). Finally, the temperature was nearly instantaneously reduced to  $T = 300$  K, quenching the system within a metastable basin on the potential-energy hypersurface.

The resulting model (model 1 in the following) remained stable while, during a run corresponding to 120 ps, 500 configurations separated by 10 time steps of 100 a.u. (24 fs) were stored for subsequent analysis. In the last run, we used the SCC correction and increased the basis set by including the d orbitals for sulphur atoms. This basis set extension provided a major improvement in the description of hypervalent sulphur molecules<sup>13</sup> as well as silicon-oxygen compounds<sup>20</sup>. While d orbitals on sulphur atoms give noticeable improvement, it appears that they are less important for arsenic and we restrict ourselves to including only s and p orbitals for the As atoms in order to speed up the calculations.

Model 1 contains three topologically identical coordination defects, namely intimate valence alternation pairs (IVAPs), where a singly coordinated sulphur atom is attached to a three-fold coordinated arsenic atom, thus increasing the coordination number of this arsenic atom to four. Apart from the IVAPs, the amorphous network is topologically ideal, in the sense that each sulphur atom is bonded to two neighbors and each arsenic atom is bonded to three. There is, however, a certain degree of chemical disorder in this system which manifests itself in the presence of nine As-As and six S-S homopolar bonds.

In the context of photoinduced metastability, a great deal of significance is attributed to the presence of topological and/or chemical defects<sup>2</sup>. It is therefore imperative to create models both with and without such defects in a theoretical investigation that attempts to be conclusive. We produced additional models by “surgically” removing the IVAP defects and homopolar bonds from model 1. Model 2, which does not contain any topological defects, was obtained by removing the three singly coordinated sulphur atoms from model 1 and rescaling this 197-atom model to the original density. This procedure did not affect the stability of the amorphous network.

In order to eliminate the chemical defects, we iteratively applied the following algorithm that utilizes the ideas<sup>21</sup> used to create models of binary amorphous solids (e.g. a-SiO<sub>2</sub>) from one-component continuous random networks (e.g. a-Si)<sup>22</sup>. First, a sulphur atom was inserted in the middle of each As-As homopolar bond. Second, each S-S bond was replaced by a single sulphur atom located at its mid-point so that each local As-S-S-As configuration turned into As-S-As. Third, the distance between each newly introduced S atom and its two nearest arsenic atoms in the newly created As-S-As units was reduced in order to increase the bonding character of the As-S bonds stretched by the above manipulation. We set a constraint on the length of the modified As-S bonds so that it did not exceed 2.5 Å. Fourth, the modified configuration was relaxed in an MD run at  $T = 300$  K for 2.5 ps, until the potential energy reached a plateau. After the first iteration, the 200-atom sample (that we call model 3 in the following) contained only one As-As and one S-S bond that were spatially well separated (the minimum As-S distance among these four atoms was 4.6 Å). Only two iterations were sufficient in order to obtain a

model with all-heteropolar bonds, which we refer to as model 4 in the following. The defect statistics for models 1-4 are summarized in Table I.

### C. Data analysis

A common way to assess the quality of a structural model is to compare experimental and calculated static structure factors. We have calculated the structure factor  $S(Q)$  by Fourier transforming the radial pair-correlation function  $g(r)$  (also often called the pair- or radial distribution function) defined as (see, e.g., Refs. 23,24,25):

$$g(r) = \frac{V}{4\pi r^2 N^2} \left\langle \sum_{i \neq j} \frac{b_i b_j}{\langle b \rangle^2} \delta(r - r_{ij}) \right\rangle, \quad (4)$$

where the sum is over all pairs of atoms in the sample of volume  $V$  separated by distance  $r_{ij}$ ,  $N$  is the total number of atoms and the angular brackets denote an ensemble average. In the case of neutron scattering, that is of interest here,  $b_i$  is the coherent scattering length of atom  $i$  and  $\langle b \rangle$  is the average scattering length. This function gives the probability of finding a pair of atoms a distance  $r$  apart, relative to the probability expected for a completely random distribution of atoms at the same density. For a binary alloy, e.g. As<sub>2</sub>S<sub>3</sub>, it is of interest to decompose  $g(r)$  in terms of the partial pair-correlation functions  $g_{\alpha\beta}(r)$ :

$$g(r) = \sum_{\alpha} \sum_{\beta} \bar{b}_{\alpha} \bar{b}_{\beta} g_{\alpha\beta}(r), \quad (5)$$

where the double sum is over atomic types and  $\bar{b}_{\alpha} = c_{\alpha} b_{\alpha} / \langle b \rangle$ , with  $c_{\alpha} = N_{\alpha} / N$  being the atomic fraction of  $\alpha$  atoms. From Eq. (4), it follows that

$$g_{\alpha\beta}(r) = \frac{V}{4\pi r^2 N^2 c_{\alpha} c_{\beta}} \left\langle \sum_{i\alpha \neq j\beta} \delta(r - r_{i\alpha, j\beta}) \right\rangle, \quad (6)$$

where the index  $i\alpha$  runs over  $\alpha$ -type atoms only. The values of the scattering lengths used here were  $b_{\text{As}} = 6.58$  fm and  $b_{\text{S}} = 2.847$  fm (see, e.g., Ref. 26). In practice, we use a standard algorithm, where the  $\delta$ -function in Eq. (6) is replaced by a function which is non-zero in a small range of separations, and a histogram is compiled of all pair separations falling within each such range (see e.g. Ref. 27). Analogously, the bond-angle distribution function can be calculated as a histogram of all bond angles in the system.

While bond-angle distributions provide information on the short-range order of an amorphous material, ring statistics have been generally used as a measure of the medium-range order. An  $n$ -membered ring is a closed loop with  $n$  atoms (or bonds). Here, we count only the shortest-path (irreducible) rings<sup>28</sup>, i.e. those which do not have “shortcuts” across them. In order to identify such rings we use the algorithm due to Franzblau<sup>28</sup>, as

implemented in the program “statrix” by Jungnickel<sup>29,30</sup>. The basic idea is to travel along the network paths (bond chains) containing a tagged atom and identify all the rings of length up to a given maximum. For each ring, it can then be verified whether it is an irreducible one (containing no cross links).

Experiments also provide information on the vibrational and electronic densities of states (VDOS and EDOS) which can be compared with the results obtained from simulation. In addition to this, simulations allow one to assess the degree of localization of the vibrational and electronic eigenstates. We compute both the vibrational and electronic densities of states by using the following definition:

$$g(\omega) = C \sum_n \delta(\omega - \omega_n), \quad (7)$$

where the constant  $C$  is determined by normalization,  $\omega_n$  are eigenfrequencies of the Hessian (dynamical) matrix of an energy-minimum configuration in the case of the VDOS or Kohn-Sham eigenfrequencies (or energies) corresponding to this configuration in the case of the EDOS, and the sum is over all eigenstates. In practice, in order to obtain a smooth representation of  $g(\omega)$ , the delta function in Eq. (7) is replaced by a Gaussian function centered at  $\omega_n$ .

In contrast to the eigenstates of a perfect crystal, that extend over the entire sample, some eigenstates in disordered solids are localized at relatively small groups of atoms. The degree of localization can be quantified by the inverse participation ratio that is defined in terms of dynamical-matrix eigenmodes or Mulliken partial charges, for vibrational or electronic excitations respectively. For a vibrational mode  $n$ , the inverse participation ratio can be defined<sup>31</sup> as

$$p_n^{-1} = \left( \sum_{i=1}^N |\mathbf{u}_i^{(n)}|^4 \right) / \left( \sum_{i=1}^N |\mathbf{u}_i^{(n)}|^2 \right)^2. \quad (8)$$

When the displacement eigenvectors  $\mathbf{u}_i^{(n)}$ ,  $n = 1, 2, \dots, 3N$ , are normalized to unity ( $\sum_i |\mathbf{u}_i^{(n)}|^2 = 1$ ),  $p_n^{-1} = 1$  for a mode totally localized at one atom and  $p_n^{-1} = 1/N$  for a completely extended mode, such as a rigid-body displacement.

In the case of the electronic properties, the linear combination of atomic orbitals (LCAO) concept employed in the DFTB program allows one to separate the contributions from individual atomic sites and orbitals to the total charge for a particular eigenstate, and to decompose the total EDOS in terms of the local electronic densities of states (LEDOS). Using the Mulliken population analysis (see, e.g., Ref. 32), the inverse participation ratio for an electronic state  $n$  can be written as<sup>7</sup>

$$p_n^{-1} = \sum_{i=1}^N |q_i^{(n)}|^2, \quad (9)$$

	Model	1	2	3	4
No. of atoms		200	197	200	200
No. of As-As bonds		9	9	1	0
No. of S-S bonds		6	6	1	0
No. of IVAPs		3	0	0	0
Total No. of defects		18	15	2	0

TABLE I: Defect statistics for models 1-4.

where the contribution to state  $n$  from atomic site  $i$ ,  $q_i^{(n)}$ , can be expressed in terms of the wavefunction coefficients in the tight-binding basis  $c_{\mu n}$  and the elements of the overlap matrix  $\mathbf{S}$ :

$$q_i^{(n)} = \sum_{\mu \in i, \nu} S_{\mu\nu} c_{\mu n} c_{\nu n} \quad (10)$$

Here, in the double sum, the index  $\mu$  runs only over the atomic orbitals located on atom  $i$  and the index  $\nu$  goes over all orbitals. As in the case of the vibrational inverse participation ratio, the electronic  $p_n^{-1}$  is equal to  $1/N$  for a totally delocalized mode and approaches unity with increasing degree of localization. The partial charges  $q_i^{(n)}$  allow one to detect on which atoms most of the charge is localized for a particular eigenstate. By refraining from summing over the atomic orbitals, i.e. over  $\mu$  in Eq. (10), one can identify the type of the atomic orbitals, e.g. s or p, most actively participating in an eigenstate. Analogously, the local EDOS for a particular orbital type can be obtained via the following expression:

$$g_\mu(\omega) = C \sum_n \delta(\omega - \omega_n) \sum_\nu S_{\mu\nu} c_{\mu n} c_{\nu n} \quad (11)$$

### III. RESULTS

#### A. Structure

By using the construction method described in Sec. II B, we obtained four models of a-As<sub>2</sub>S<sub>3</sub> which are distinguished by the presence and concentration of topological and chemical defects (see Table I). We also created 60- and 100-atom models with similar concentrations of homopolar bonds as in models 1 and 2, and without coordination defects.

Fig. 1(a) shows that the pair-correlation function (PCF) corresponding to model 1 compares well with two independent neutron-scattering experimental results. The discrepancy between the two experimental PCFs allows one to estimate the uncertainty in the experimental data. The main difference between the experimental and simulated results is in the height of the first peak. Since the experimental PCFs are obtained by Fourier transforming the measured static structure factor, where the large- $Q$  oscillations are damped by applying a window

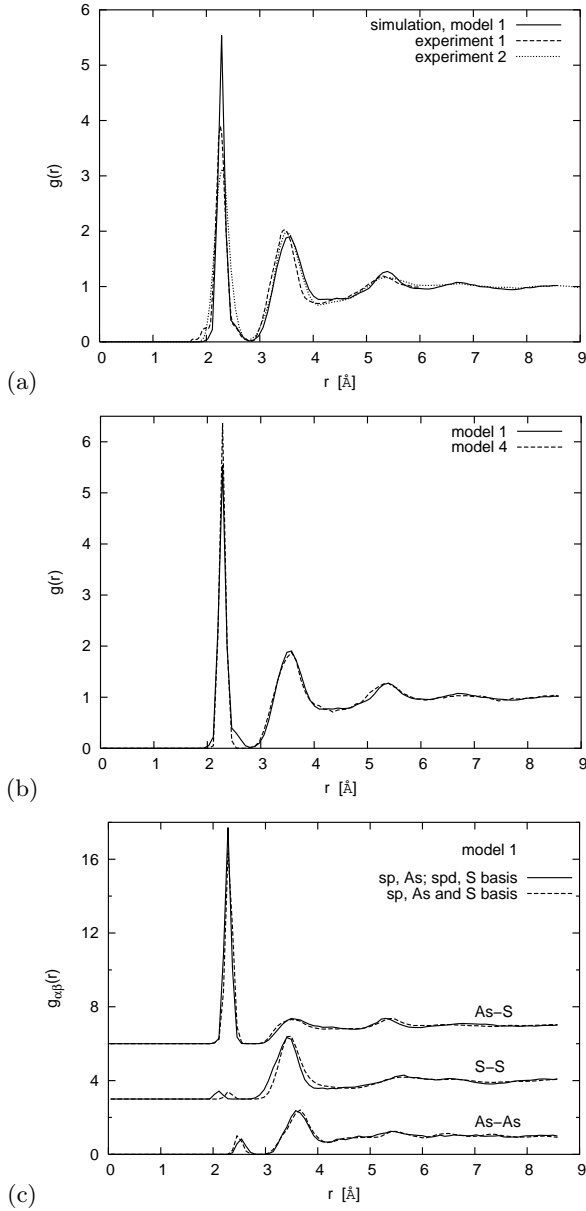


FIG. 1: (a) Total pair-correlation functions for model 1 and the neutron-diffraction experiments 1 (Ref. 12) and 2 (Ref. 18). (b) Total pair-correlation functions for models 1 (the same as in (a)) and 4. (c) Partial pair-correlation functions for model 1.  $g_{\text{S-S}}(r)$  and  $g_{\text{As-S}}(r)$  are shifted upwards by 3 and 6 units, respectively.

function, this reduces the height of the first peak in  $g(r)$  and also broadens its width.

Although the PCFs corresponding to models 2-4 are quite similar to that for model 1 (which is why we do not show here the PCFs for models 2 and 3), there is one conspicuous distinction in the shape of the first peak that depends on whether or not the system contains homopolar bonds (see Fig. 1(b)). While this peak is symmetric for model 4 with all heteropolar bonds, there is a shoulder on either side of the peak in the PCF for model 1. From

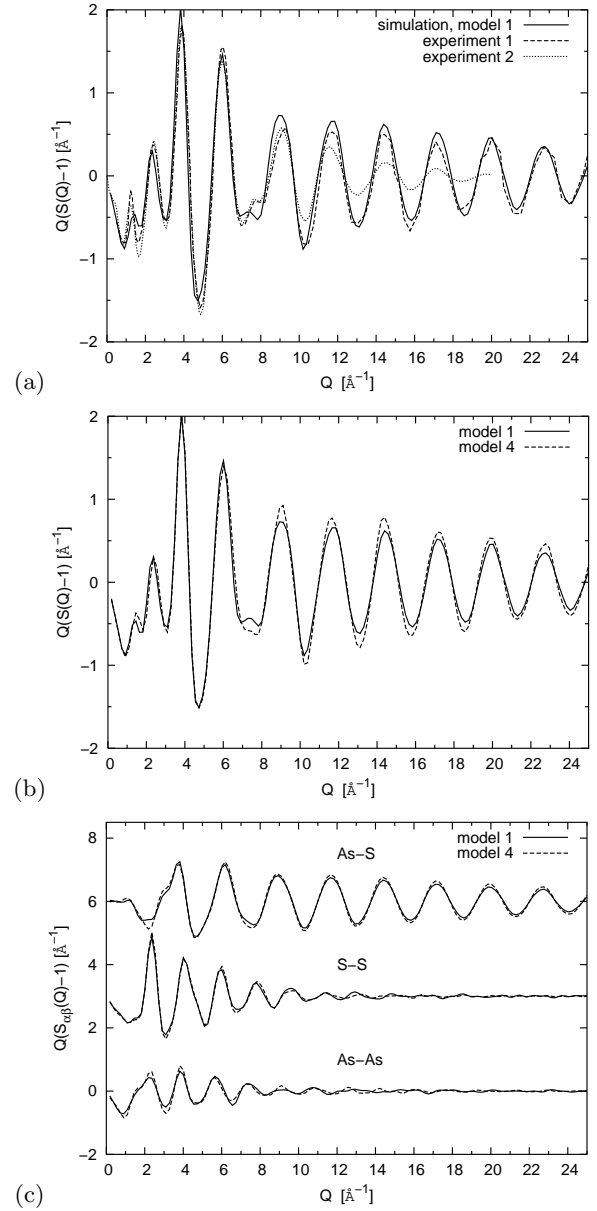


FIG. 2: (a) Reduced structure factors (interference functions) for model 1 and the neutron-diffraction experiments 1 (Ref. 12) and 2 (Ref. 18). (b) Total interference functions for models 1 (the same as in (a)) and 4. (c) Partial interference functions for models 1 and 4. The functions corresponding to S-S and As-S correlations are shifted upwards by 3 and 6 units, respectively.

Fig. 1(c), it is seen that the shoulders in the first peak of the total PCF originate from the homopolar As-As and S-S bonds which produce small peaks in the respective partial PCFs at this position. It is remarkable that the calculated PCF for model 1 virtually reproduces the right-hand side of the first peak in the PCF from experiment 1 (see Fig. 1(a)). This result supports one of the conclusions of Ref. 12 (experiment 1) that the low- and high- $r$  sides of the base of the first peak in the PCF can

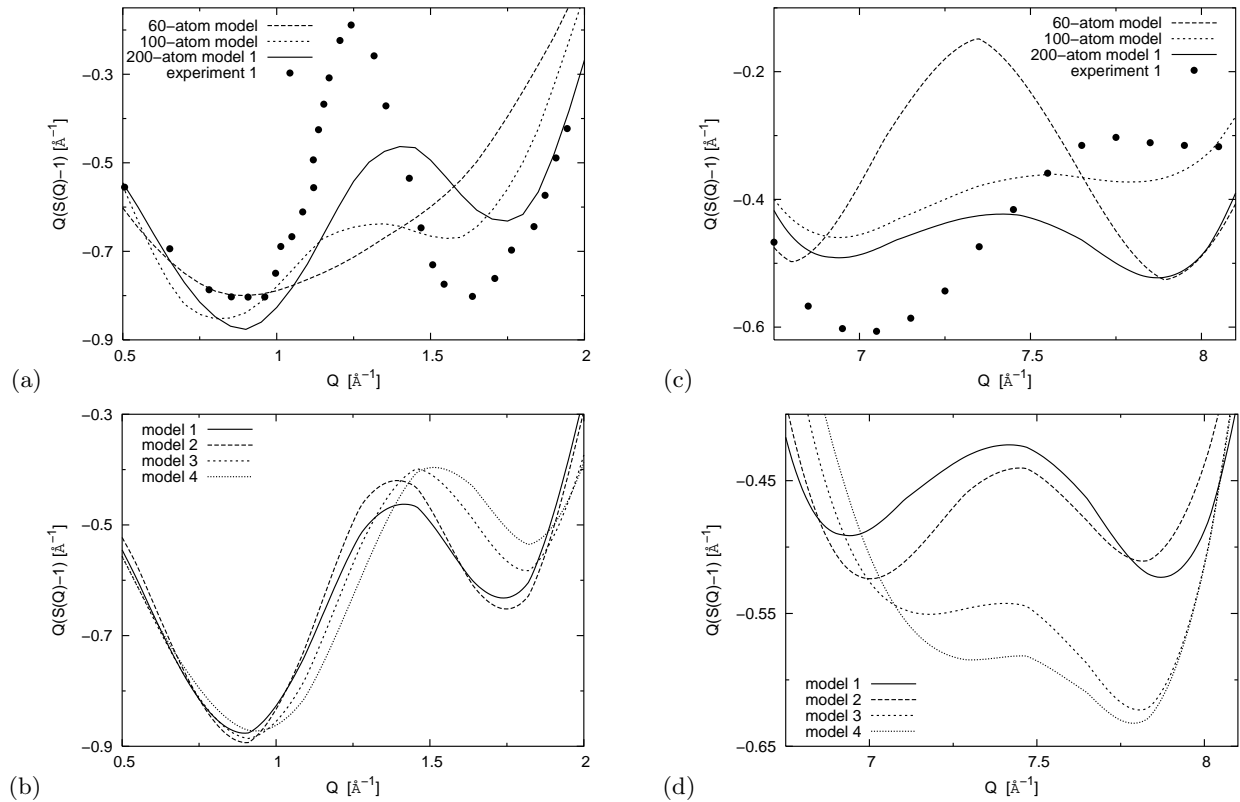


FIG. 3: Close-up of the parts of  $F(Q) = Q(S(Q) - 1)$  most sensitive to changes in the local structure. The FSDP region for (a) the 60- and 100-atom models, model 1 and experiment 1, and (b) models 1-4, respectively. The region near  $Q \approx 7.5 \text{ \AA}^{-1}$  for (c) the 60- and 100-atom models, model 1 and experiment 1, and (d) models 1-4, respectively.

Sample	$r_{\text{As-S}} [\text{\AA}]$	$Z_{\text{As-S}}$	$Z_{\text{S-As}}$
experiment 1	2.27	2.8	1.8
model 1	2.279	2.81	1.88

TABLE II: Values of average bond length and coordination numbers for the first coordination shell found from peak fitting (experiment 1) and direct calculation (model 1).

be ascribed to S-S and As-As bonds, respectively. Table II further demonstrates that the agreement between the structural characteristics of model 1 and experiment 1 is very good and, in particular, that the As-S coordination numbers for these two samples are practically the same. The larger discrepancy in the S-As coordination number and the low- $r$  side of the first peak in the PCF arises from the relatively small system size and the fact that the numbers of As-As (nine) and S-S (six) homopolar bonds are not equal to each other in model 1. The position of the first peak in the partial PCF  $g_{\text{S-S}}(r)$  also plays a role here. As is seen from Fig. 1(c), this peak shifts towards the low- $r$  end when d orbitals on sulphur atoms are included into the basis set. When a  $T = 300 \text{ K}$  run is performed without the d orbitals in the basis set, the position of the first peak in  $g_{\text{S-S}}$  coincides with that

of the first peak in  $g_{\text{As-S}}$ , and the shoulder on the low- $r$  side of the simulated total  $g(r)$  is not seen at all.

It is instructive to compare the structural data also in  $Q$ -space, as this often emphasizes features that are not obvious in an  $r$ -space representation. Fig. 2(a) shows the reduced structure factors (or interference functions)  $F(Q) = Q(S(Q) - 1)$ , related to the PCFs in Fig. 1(a) by a Fourier transform. Again, the agreement between model 1 and experiment 1 is very good. From the rate of decay of  $F(Q)$  from experiment 2, it is apparent that the data in Ref. 18 are reported for  $F(Q)$  multiplied by a window function.

$F(Q)$  for model 1 exhibits a first-sharp diffraction peak (FSDP) at about the same position,  $Q \approx 1.5 \text{ \AA}^{-1}$ , as found in the experiments. The magnitude of this peak depends on the system size and is expected to increase for a larger model. This statement is supported by the observation of this tendency as the peak develops in our 60-, 100-, and 200-atom models (see Fig. 3(a)). Fig. 3(b) demonstrates a systematic displacement in the position of the FSDP towards the high- $Q$  end as the number of defects is reduced from model 1 to model 4. In Ref. 33, it was observed that the FSDP in X-ray diffraction intensity curves for an a- $\text{As}_2\text{S}_3$  thick ( $8 \mu\text{m}$ ) film reversibly moved towards the low- and high- $Q$  end upon illumination and annealing, respectively. The result in Fig. 3(b)

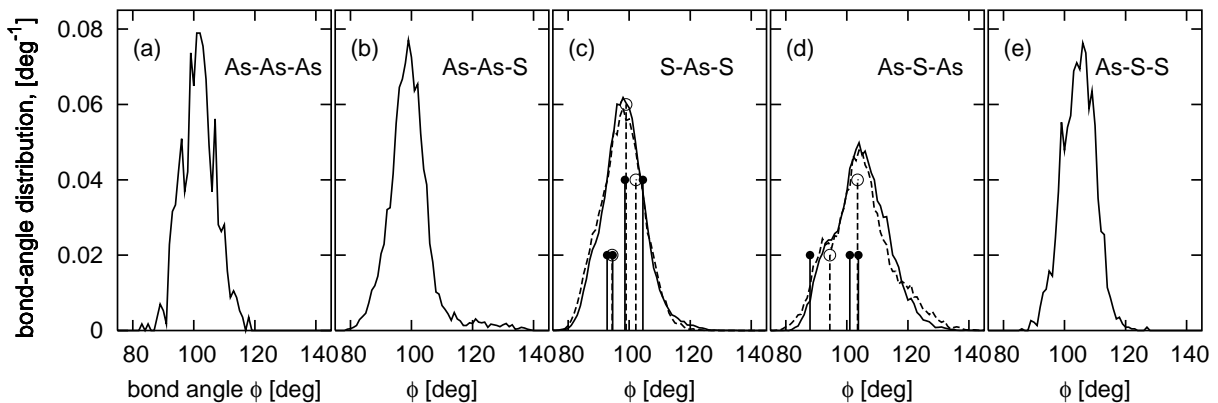


FIG. 4: Bond-angle distributions. Solid lines in (a)-(e) and dashed lines in (c) and (d) correspond to models 1 and 4 respectively. The height of vertical lines topped by circles is proportional to the number of distinct angles within one degree in the crystal structure of orpiment. Solid vertical lines and circles correspond to the experimental data from the crystallographic database and Ref. 16, and the dashed vertical lines and open circles correspond to the structure optimized by the DFTB method.

is consistent with the above observation, if we suppose that the defect concentration is reversibly increased and decreased upon illumination and annealing, respectively. The height of the measured<sup>33</sup> peak, however, increased as its position wavenumber,  $Q_1$ , decreased after illumination, while in the simulations we observed the opposite tendency for the height of the FSDP to increase upon elimination of defects and increasing  $Q_1$ . A possible reason for the different behavior of the height of the FSDP is that the simulations of the bulk  $\alpha$ - $\text{As}_2\text{S}_3$  were performed at constant volume, while the experiment was done for an amorphous film at atmospheric pressure.

Another distinction between the different interference functions presented in Fig. 2 is seen in the range  $7 \text{ \AA}^{-1} \lesssim Q \lesssim 8 \text{ \AA}^{-1}$ .  $F(Q)$  appears to be very sensitive to structural differences in this particular range of wavenumbers, as is apparent from Fig. 2(b), where the interference function for model 1 is compared with that for model 4, and from Fig. 3(c,d), where  $F(Q)$  is magnified in this  $Q$ -interval, and the differences between the curves are prominent. Although the differences between the partial interference functions for models 1 and 4 (shown in Fig. 2(c)) are each rather subtle in this  $Q$ -interval, they become more pronounced when combined into the total  $F(Q)$  (see Fig. 2(b)). The small peak, which is seen in  $F(Q)$  for model 1 at  $Q \approx 7.5 \text{ \AA}^{-1}$ , diminishes from model 1 to 4, so that it is practically not seen in the case of the stoichiometric model 4 (see Fig. 3(d)). The presence and position of this small peak may be attributed to the presence and spatial distribution, respectively, of homopolar bonds in the system. Similar peaks are seen in  $F(Q)$  at about  $Q = 7.5 \text{ \AA}^{-1}$  for both experiments mentioned here (Fig. 2(a), Refs. 12,18) and in the experiment reported in Ref. 11. While, in all these independent experiments, these peaks virtually coincide, in the different models presented here they do not agree so well (see Fig. 3(c)), as, perhaps, can be expected in the case of small system sizes.

Another structural characteristic that is of interest, and that is easily accessible in computer simulations, is the bond-angle distribution (see Fig. 4). Although we have no experimental data for this distribution, the known structure of a corresponding crystal can serve as a guide in assessing the quality of our models — many statistical distributions associated with amorphous models agree overall with the respective broadened distributions for the counterpart crystals (see, e.g., Refs. 34,35), which also applies to the bond-angle distributions presented here. In addition to this, Fig. 4(c),(d) shows that the geometry optimization with DFTB results in a crystal structure that agrees with the experimental one to within about two percent, not only in bond distances and lattice constants, but also in bond angles.

It may appear reasonable to ascribe the asymmetry of the distributions for S-As-S and As-S-As angles in the form of the shoulders on the low-angle side to the presence of four-membered As-S-As-S rings, as has been observed in tetrahedrally bonded chalcogenide semiconductors, e.g.  $\text{GeS}_2$ <sup>17</sup>. Although such four-membered rings would definitely contribute to the low-angle part of the distribution due to geometrical constraints, their number in our models is not so large (see Table III) and, for that reason, the relative fraction of angles involved in these rings is rather small (about 7 % of S-As-S angles and 13 % of As-S-As angles). We therefore conclude that the asymmetry of the heteropolar bond-angle distributions is inherent to this type of material, as is evidenced in the case of both crystal and amorphous structures.

Interestingly, there are no 12-membered rings in our models of  $\alpha$ - $\text{As}_2\text{S}_3$ , while only such rings exist in the crystal structure of orpiment. This is another strong piece of evidence that models 1-4 do not contain any memory of the initial crystalline atomic arrangement. Also there are no three-membered rings, that were previously reported to be found in a model of  $\alpha$ - $\text{As}_2\text{Se}_3$ <sup>8</sup>, whose presence would contribute a few small angles and would increase



ring size $n$	4	5	6	8	10	14	15	16	18	19	20	21	22
models 1, 2	5	6	1	1	1	2	2	3	1	2	6	1	1
model 3	8	0	5	1	1	2	2	3	4	0	6	0	3
model 4	8	0	5	1	1	2	0	5	4	0	6	0	3

TABLE III: Ring statistics - number of  $n$ -membered shortest path<sup>28</sup> rings for  $n \leq 22$ . Columns containing only zeros are not included.

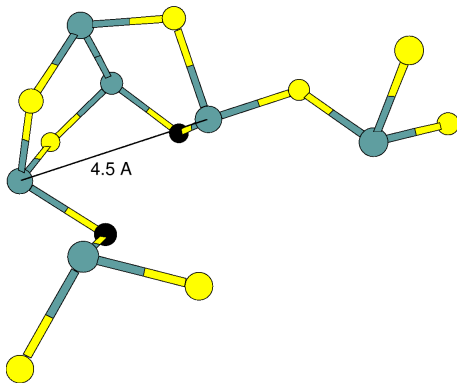


FIG. 5: Fragment of model 1: two bond-sharing five-membered rings and the two  $\text{AsS}_3$  groups connected to this structure. The shading of the As atoms (all with three neighbors) is darker than that of the S atoms (all with two neighbors). The HOMO level is mostly localized on the two S atoms that are marked black. The distance between these two atoms is  $3.42 \text{ \AA}$ .

the number of homopolar bonds.

Special significance can be attributed to the presence of five-membered rings in models 1 and 2 with an appreciable concentration of homopolar bonds (models with all-heteropolar bonds contain only an even number of atoms in all rings). When such rings share some of the bonds, the resulting local structure is close to that of cage-like molecules (e.g.  $\text{As}_4\text{S}_4$  or  $\text{As}_4\text{S}_3$ ), as found in the vapor phase and in some chalcogenide molecular crystals. Fig 5 (cf. Fig. 8.8(b) in Ref. 36) shows two such bond-sharing rings. Upon breaking the two bonds connecting the rings to the rest of the network, the distance of  $4.54 \text{ \AA}$  between the two freed arsenic atoms could be reduced, thus producing another As-As homopolar bond and this group of atoms would then form an  $\text{As}_4\text{S}_4$  molecule. Evidence of the presence of such molecules in bulk  $\text{As}_x\text{S}_{1-x}$  glasses from Raman-scattering experiments has recently been reported in Ref. 37. Our result shows that the  $\text{As}_4\text{S}_4$  fragments may not only form discrete cage-like molecules but also be embedded into the amorphous network. We verified that the vibrational signatures of the  $\text{As}_4\text{S}_4$  fragment from models 1 and 2 are similar to those from an isolated  $\text{As}_4\text{S}_4$  molecule, apart from a few very symmetric modes of the latter.

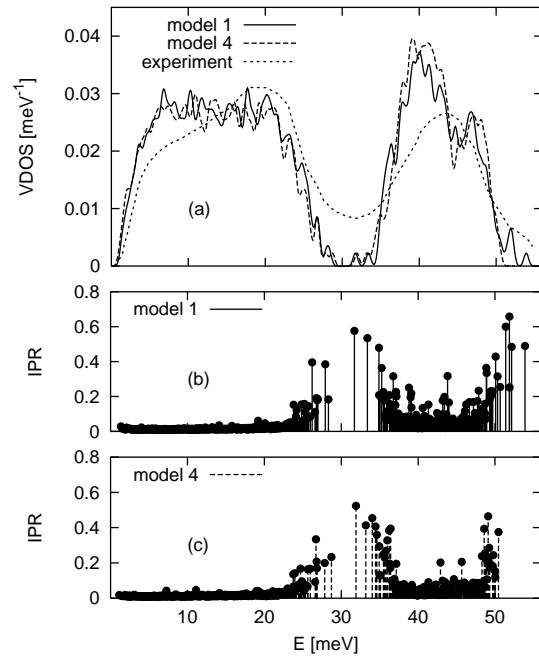


FIG. 6: Vibrational densities of states (a) and inverse participation ratios (b),(c) for models 1 and 4. The experimental data in (a) are obtained from Ref. 38.

## B. Vibrational properties

The vibrational density of states (VDOS) for models 1 and 4 is shown in Fig. 6(a). It has the two-band form generally observed in amorphous semiconductors. The vibrational spectrum for our models is essentially superimposable on the calculated VDOS<sup>8</sup> for a model of  $a\text{-As}_2\text{Se}_3$  if the energy in Fig. 6(a) is downscaled by a factor of about 0.67. All main features — the position of the gap between the acoustic and optic bands, as well as the relative width and height of VDOS within these bands — agree with available inelastic neutron-scattering experimental data<sup>11,38</sup>. Note that the experimental curve in Fig. 6(a) corresponds to a measurement at room temperature, whereas the results obtained from simulation are calculated for an energy-minimum configuration in the harmonic approximation. An attempt to measure the VDOS of  $a\text{-As}_2\text{S}_3$  at temperatures as low as 25 K was made in Ref. 11, and the tendency for the narrowing and heightening of the optic band and the flattening of the top of the acoustic band was captured, although the experimental uncertainty was rather large.

The inverse participation ratios (IPR) (see Fig. 6(b),(c)) show that the vibrational eigenmodes are significantly localized in the gap between the acoustic and optic bands, and the high- $E$  end of the spectrum. The first three highest energy modes in model 1 are localized on S-S bonds, while the next two (with the largest IPR) are localized on IVAPs. The VDOS's for models 1 and 4 differ mainly in the

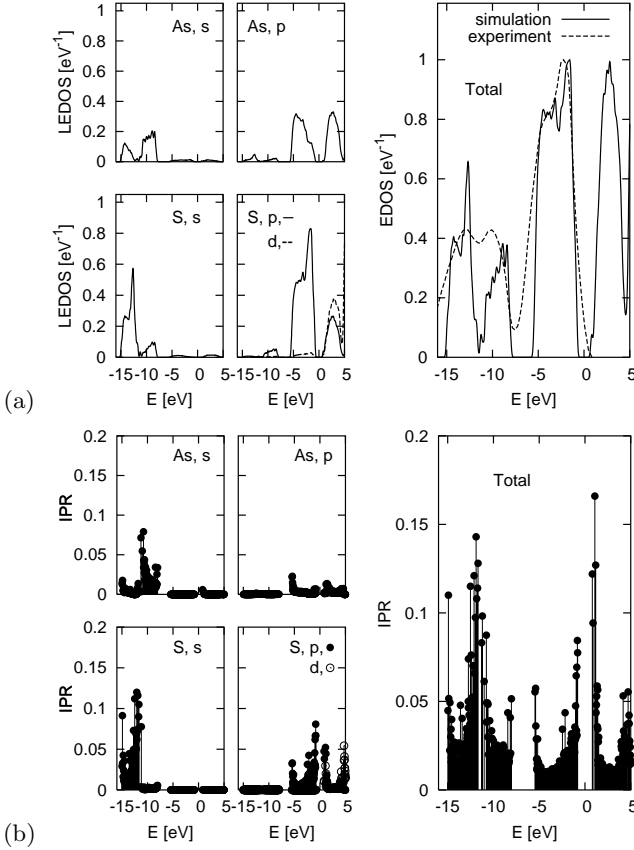


FIG. 7: Local and total electronic density of states (a) and inverse participation ratios (b) for model 1. The Fermi energy is at the origin. The experimental data in (a) are obtained from Ref. 39.

absence of the just-mentioned highest energy modes from the spectrum corresponding to the stoichiometric model 4. The highest energy mode ( $E = 50.5$  meV) in model 4 is localized on a relatively complex structure involving three  $\text{AsS}_3$  pyramids in a chain  $\text{As-S-As-S-As}$ , where both  $\text{As-S-As}$  angles ( $118$  and  $122^\circ$ ) are at the large- $\phi$  end of the bond-angle distribution shown in Fig. 4(d). Within the optic band, the modes with IPR greater than 0.2, at  $E = 43.8$  meV in model 1 and at  $E = 42.9$  and  $45.7$  meV in model 4, are localized at four-membered rings. In the band gap, the mode at the top of the acoustic band in model 1 is localized on an  $\text{As-As-S-S}$  chain, and the mode at the bottom of the optic band is localized on an IVAP. The mode at the top of the acoustic band in model 4 is predominantly localized on a four-membered ring, and the mode at the bottom of the optic band is almost entirely localized on a six-membered ring.

### C. Electronic structure

The electronic density of states for model 1, as well as the inverse participation ratios for these states, are

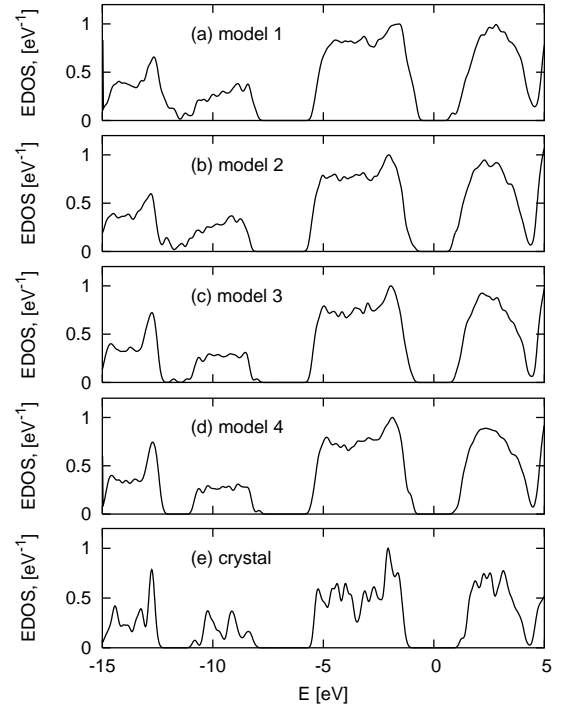


FIG. 8: Electronic densities of states of the models of  $\alpha\text{-As}_2\text{S}_3$  and orpiment.

shown in Fig. 7. The calculated total EDOS is in good agreement with the density of valence states<sup>39</sup> measured by X-ray photoemission spectroscopy. The total EDOS is also very similar to that of arsenic selenide in Ref. 8, where an experimental result<sup>40</sup> for that material was presented to be in agreement with the calculated one.

The local EDOS's for different elements and orbital types, shown in Fig. 7(a), confirm the analysis presented in Ref. 39. The top of the valence band is due to the non-bonding lone-pair p orbitals of the S atoms, and the rest of the valence band is attributed to the bonding p orbitals on the S and As atoms.

The s band is composed of two sub-bands. The low- $E$  sub-band at about  $-(15-12)$  eV is essentially an s type sulphur band, and the sub-band at about  $-(12-8)$  eV is predominately due to the arsenic s orbitals. In Ref. 8, the fact that the s band of selenium is below the s band of arsenic was attributed to the greater nuclear charge of Se. Since the electronic structure of arsenic sulphide, a compound containing a much lighter chalcogen, virtually coincides with that for arsenic selenide, the above explanation is incorrect. A strong repulsion between As and S/Se s levels due to chemical ordering is more likely to be responsible for the separation of the s band into high (As) and low (S/Se) sub-bands<sup>39</sup>. Note that the two s sub-bands are perfectly separated only when the chemical ordering is perfect, i.e. in models with all-heteropolar bonds, as seen in Fig. 8(d,e). The degree of admixture of As and S s orbitals within the low and high sub-bands, respectively, is about 30 % (see the “As, s” and “S, s”

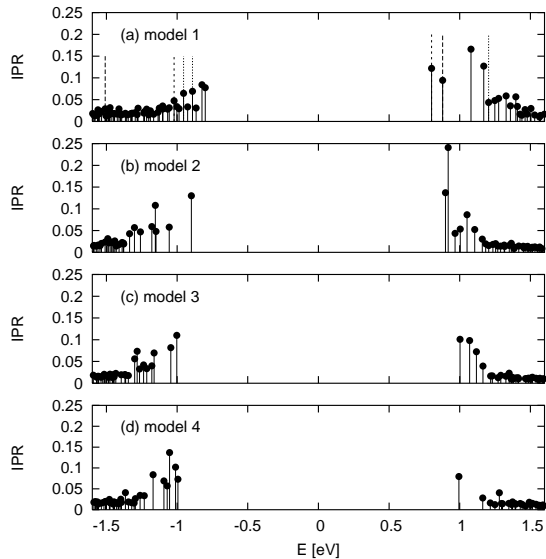


FIG. 9: Inverse participation ratios at the band edges for all the four models. The vertical dashed lines in (a) demarcate the levels mostly localized at IVAPs, with each line type corresponding to the same IVAP.

model	1	2	3	4	crystal
$E(\text{LUMO})-E(\text{HOMO})$	1.60	1.80	2.00	1.99	2.51
half-maximum gap	2.67	2.72	2.74	2.74	3.13

TABLE IV: Band-gap energies in eV estimated as the differences between the LUMO and HOMO eigenvalues and as the differences of the band-gap edges at the level  $0.5 \text{ eV}^{-1}$  in EDOS normalized so that the maximum value within the valence band is equal to unity.

panels in Fig. 7(a)), again in agreement with Ref. 39.

The conduction band is composed of about equal contributions from the antibonding As and S p orbitals and the S d orbitals. Perhaps, if the As d orbitals were included in the basis set, there would be a contribution from them too. While this might not significantly affect the structural and ground-state electronic properties of our models, this remark could be of greater importance for excited-state simulations.

The EDOS's for models 1-4 and for the crystal structure of orpiment are plotted in Fig. 8. It is seen that the overall similarity is preserved for all these structures. The main differences among the EDOS's corresponding to the amorphous structures are the widening of the optical band gap (see also Table IV) and the clearing of the gap within the low-energy s-band as the number of defects diminishes.

Localization of the electronic states near the optical band-gap edges is of great interest for studies of photoinduced phenomena. A close-up of the inverse participation ratios at energies near the band edges for models 1-4 is

shown in Fig. 9. If topological (or coordination) defects are present in a model, as in model 1, some of the states, especially at the bottom of the conduction band, are localized at them (see Fig. 9(a)). This tendency was also emphasized in Ref. 8. A comparable, or even greater degree of localization, is observed in model 2 (see Fig. 9(b)) where there are no coordination defects, but there is an appreciable concentration of homopolar bonds (or chemical defects). As the number of chemical defects goes to zero from model 2 to model 4, it is seen that localization at the top of the valence band remains qualitatively similar, whereas at the bottom of the conduction band it becomes less pronounced (see Fig. 9(b)-(d)).

The general picture is that, at the top of the valence band, the eigenstates are predominantly localized at what can be called sulphur-rich regions, where several sulphur atoms are closer than about  $3.45 \text{ \AA}$ , i.e. their interatomic distances are on the low- $r$  side of the second peak in  $g_{\text{S-S}}(r)$  shown in Fig. 1(c) or some of these atoms form homopolar S-S bonds. For instance, most of the HOMO level in model 1 is localized at two sulphur atoms separated by  $3.42 \text{ \AA}$  and which are part of the molecule-like fragment depicted in Fig. 5. By inspecting the projected (local) IPRs in Fig. 7(b) at the optical gap edges, it is seen that the IPRs are greatest for the S atoms. It appears that the localization at the top of the valence band is facilitated by the proximity of the lone-pair p orbitals in the sulphur-rich regions.

At the bottom of the conduction band, the states tend to localize at four-membered rings in all models, and at S-S homopolar bonds (some of these bonds are in five-membered rings) and IVAPs when such defects are present. In model 4, all three conduction-band states with an IPR greater than 0.025 (see Fig. 9(d)) are localized at four-membered rings.

#### IV. CONCLUSION

We have generated several models of amorphous arsenic sulphide by using a density-functional-based tight-binding method. All models agree very well with the neutron-scattering experimental structural data. We observe a tendency for formation of quasi-molecular structural groups which suggests that amorphous chalcogenides can be viewed as nanostructured materials. Vibrational properties are also in agreement with experimental results.

In models containing both homopolar bonds and topological defects, a significant degree of electronic-state localization has been observed near both band-gap edges. Although the coordination-number defects are optically active, their presence may not be necessary for exhibiting photostructural changes when there is a sufficient concentration of homopolar bonds in the material. This statement is supported by the observation that, upon removal of the coordination defects from the system, the degree of electronic-state localization is not reduced in the resul-

tant continuous network model with homopolar bonds. Furthermore, the valence-alternation defect concentration is estimated to be rather small ( $10^{17} \text{ cm}^{-3}$  in Ref. 19) compared to the atomic density of about  $2 \times 10^{25} \text{ cm}^{-3}$ . This indicates that, in the volume occupied by our 200-atom models, it is less likely to find a topological defect than to come across none.

A stoichiometric continuous network model has allowed us to identify the structural motifs where electronic eigenstates predominantly localize at the optical band edges, in the absence of coordination and chemical defects. These are sulphur-rich regions for the top of the valence band and four-membered rings for the bottom of the conduction band. Electronic properties of this glass model with all-heteropolar bonds are very similar to those of the corresponding crystalline phase, orpiment, most notably the clean gaps in both s and p bands. Although the valence band in this case contains about as many localized states as in models with defects, the conduction band has very few of them. It is expected that, if there were no four-membered rings in this structure, all states in the conduction band would be virtually delocalized.

Therefore we conclude that perhaps the dominant contribution to photo-induced effects originates from the presence of electronic states localized in the vicinity of homopolar bonds, in support of the theoretical models where the photo-induced structural changes are attributed to the presence of homopolar bonds in these materials (see, e.g., Refs. 2,41). Although electronic states can also localize in all-heteropolar regions and in the vicinity of the topological defects, the contribution of such states is likely to be rather small due to the low degree of localization in the conduction band and the low concentration of such defects, respectively. Verification of this conjecture requires excited-state calculations and is beyond the scope of the present paper. We plan to do these calculations in the future.

### Acknowledgments

S.I.S. is grateful to the EPSRC for financial support. We thank the British Council and DAAD for provision of financial support.

\* Electronic address: sis24@cam.ac.uk

- <sup>1</sup> H. S. Nalwa, ed., *Handbook of Advanced Electronic and Photonic Materials and Devices*, vol. 5: Chalcogenide Glasses and Sol-Gel Materials (Academic Press, San Diego, 2001).
- <sup>2</sup> A. V. Kolobov, ed., *Photo-Induced Metastability in Amorphous Semiconductors* (Wiley-VCH, Weinheim, 2003).
- <sup>3</sup> J. M. Lee, M. A. Paesler, D. E. Sayers, and A. Fontaine, *J. Non-Cryst. Solids* **123**, 295 (1990).
- <sup>4</sup> A. J. Lowe, S. R. Elliott, and G. N. Greaves, *Philos. Mag. B* **54**, 483 (1986).
- <sup>5</sup> H. Fritzsche, in *Insulating and Semiconducting Glasses*, edited by P. Boolchand (World Scientific, Singapore, 2000), vol. 17 of *Series on Directions in Condensed Matter Physics*, pp. 653–690.
- <sup>6</sup> S. Ovshinsky, in *Insulating and Semiconducting Glasses*, edited by P. Boolchand (World Scientific, Singapore, 2000), vol. 17 of *Series on Directions in Condensed Matter Physics*, pp. 729–779.
- <sup>7</sup> M. Cobb, D. A. Drabold, and R. L. Cappelletti, *Phys. Rev. B* **54**, 12162 (1996).
- <sup>8</sup> J. Li and D. A. Drabold, *Phys. Rev. B* **61**, 11998 (2000).
- <sup>9</sup> J. Li and D. A. Drabold, *Phys. Rev. Lett.* **85**, 2785 (2000).
- <sup>10</sup> T. Frauenheim, G. Seifert, M. Elstner, T. Niehaus, C. Köhler, M. Amkreutz, M. Sternberg, Z. Hajnal, A. D. Carlo, and S. Suhai, *J. Phys.: Condens. Matter* **14**, 3015 (2002).
- <sup>11</sup> A. Haar, Ph.D. thesis, Cambridge University (2000).
- <sup>12</sup> J. H. Lee, A. C. Hannon, and S. R. Elliott, *Neutron scattering studies of arsenic sulphide glasses*, unpublished.
- <sup>13</sup> T. Niehaus, M. Elstner, T. Frauenheim, and S. Suhai, *J. Mol. Struct. THEOCHEM* **541**, 185 (2001).
- <sup>14</sup> D. Porezag, T. Frauenheim, T. Köhler, G. Seifert, and R. Kaschner, *Phys. Rev. B* **51**, 12947 (1995).
- <sup>15</sup> M. R. Pederson, D. V. Porezag, J. Kortus, K. Jackson, and D. Patton, *The NRLMOL homepage*, URL <http://cst-www.nrl.navy.mil/~nrlmol/>.
- <sup>16</sup> D. J. E. Mullen and W. Nowacki, *Z. Kristallogr.* **136**, 48 (1972).
- <sup>17</sup> S. Blaineau, P. Jund, and D. A. Drabold, *Phys. Rev. B* **67**, 094204 (2003).
- <sup>18</sup> Y. Iwadate, T. Hattori, S. Nishiyama, K. Fukushima, Y. Mochizuki, M. Misawa, and T. Fukunaga, *J. Phys. Chem. Solids* **60**, 1447 (1999).
- <sup>19</sup> A. Feltz, *Amorphous Inorganic Materials and Glasses* (VCH, Weinheim, 1993), p. 203.
- <sup>20</sup> R. Kaschner, T. Frauenheim, T. Köhler, and G. Seifert, *Journal of Comp.-Aided Material Design* **4**, 53 (1997).
- <sup>21</sup> N. Mousseau, private communication.
- <sup>22</sup> G. T. Barkema and N. Mousseau, *Phys. Rev. B* **62**, 4985 (2000).
- <sup>23</sup> J.-P. Hansen and I. R. McDonald, *Theory of Simple Liquids* (Academic Press, London, 1986), 2nd ed.
- <sup>24</sup> D. A. McQuarrie, *Statistical Mechanics* (University Science Books, 2000).
- <sup>25</sup> Y. Waseda, *The Structure of Non-Crystalline Materials* (McGraw-Hill, New York, 1986).
- <sup>26</sup> *Neutron scattering lengths and cross sections*, NIST Center for Neutron Research, <http://www.ncnr.nist.gov/resources/n-lengths/>.
- <sup>27</sup> M. P. Allen and D. J. Tildesley, *Computer Simulation of Liquids* (Clarendon Press, Oxford, 1987).
- <sup>28</sup> D. S. Franzblau, *Phys. Rev. B* **44**, 4925 (1991).
- <sup>29</sup> G. Jungnickel, unpublished.
- <sup>30</sup> G. Jungnickel, T. Frauenheim, D. Porezag, P. Blaudeck, and U. Stephan, *Phys. Rev. B* **50**, 6709 (1994).
- <sup>31</sup> R. J. Bell and P. Dean, *Philos. Mag.* **25**, 1381 (1972).
- <sup>32</sup> A. Szabo and N. S. Ostlund, *Modern Quantum Chem-*

- istry: Introduction to Advanced Electronic Structure Theory* (McMillan, New York, 1982).
- <sup>33</sup> K. Tanaka, Appl. Phys. Lett. **26**, 243 (1975).
- <sup>34</sup> S. I. Simdyankin, S. N. Taraskin, M. Dzugutov, and S. R. Elliott, Phys. Rev. B **62**, 3223 (2000).
- <sup>35</sup> S. I. Simdyankin, S. N. Taraskin, M. Elenius, S. R. Elliott, and M. Dzugutov, Phys. Rev. B **65**, 104302 (2002).
- <sup>36</sup> S. N. Yannopoulos, in *Photo-Induced Metastability in Amorphous Semiconductors*, edited by A. V. Kolobov (Wiley-VCH, Weinheim, 2003), p. 134.
- <sup>37</sup> D. G. Georgiev, P. Boolchand, and K. A. Jackson, cond-mat/0308094 (2003).
- <sup>38</sup> S. L. Isakov, S. N. Ishmaev, V. K. Malinovsky, V. N. Novikov, P. P. Parshin, S. N. Popov, A. P. Sokolov, and M. G. Zemlyanov, Solid State Communications **86**, 123 (1993).
- <sup>39</sup> S. G. Bishop and N. J. Shevchik, Phys. Rev. B **12**, 1567 (1975).
- <sup>40</sup> K. S. Liang, J. Non-Cryst. Solids **18**, 197 (1975).
- <sup>41</sup> O. I. Shpotyuk, Opto-Electron. Rev. **11**, 19 (2003).